Journal of Alloys and Compounds 1079 (2026) 189991

Contents lists available at ScienceDirect

Journal of Alloys and Compounds

journal homepage: www.elsevier.com/locate/jalcom

Charge-transport-tailoring via sulfonic acid ligands for high performance perovskite quantum dots light-emitting diodes

Maolin Mu [a,1], Lunyao Pan [b,1], Xiankan Zeng [a], Yaolin Zhang [c], Yuqiang Huang [c], Chenglong Li [a], Di Shen [a], Xinning Wang [a], Weiqing Yang [a,d], Fangyan Liu [e,*], Wen Li [a,*]

[a] Key Laboratory of Advanced Technologies of Materials (Ministry of Education), School of Materials Science and Engineering, Southwest Jiaotong University, Chengdu 610031, PR China
[b] School of Optoelectronic Science and Engineering, University of Electronic Science and Technology of China, Chengdu 611731, PR China
[c] College of Science, Northeast Forestry University, Harbin, Heilongjiang 150040, PR China
[d] Research Institute of Frontier Science, Southwest Jiaotong University, Chengdu 610031, PR China
[e] School of Electrical Engineering, Southwest Jiaotong University, Chengdu, China

ARTICLE INFO

Keywords:
Sulfonic acid ligands
Cu_2ZnSnS_4
Carrier transport
Perovskite quantum dots light-emitting diodes

ABSTRACT

Lead halide perovskite quantum dots (PeQDs) have become highly competitive electroluminescent materials for light-emitting diodes, primarily owing to their tunable emission wavelength, narrow emission full-width at half-maximum, high defect tolerance, and cost-effective solution processability. However, the inherently insulating long-chain organic ligands on PeQDs surface tend to induce abundant defects and imbalanced charge transport in PeQDs light-emitting diodes (PeQLEDs). To address this issue, we develop a ligand-mediated strategy for the surface reconstruction of $FAPbBr_3$ QDs using benzene sulfonic acid and p-toluenesulfonic acid (DBSA). Specifically, the more strongly polarized DBSA molecules exhibit a pronounced delocalized electron cloud distribution, which promoted more efficient carrier transport and significantly improved the carrier mobility of PeQDs film. Consequently, the DBSA optimized PeQLEDs exhibits stable electroluminescence emission at 529 nm with a maximum external quantum efficiency of up to 17.44% as well as a low turn-on voltage of 2.2 V and a maximum luminance of 45069 cd m^{-2}. These values are all substantially superior to those of the control device. This work provides new insights into the exploration of appropriate surface ligands for regulating the surface electrical properties of PeQDs and modulating carrier transport in optoelectronic devices, thereby advancing the development of high-performance PeQLEDs.

1. Introduction

Metal halide perovskite quantum dots (PeQDs) have emerged as competitive candidates for optoelectronic devices due to their tunable bandgap, narrow emission spectra, high defect tolerance, and cost-effective solution-processability [1–4]. Currently, PeQDs have been extensively applied in various thin-film optoelectronic devices, including light-emitting diodes (LEDs), solar cells, and photodetectors [5–7]. Especially in the field of LEDs, perovskite quantum dot LEDs (PeQLEDs) has been achieved notable progress in recent years, the external quantum efficiencies (EQEs) of blue, green, and red PeQLEDs have surpassed 26%, 30%, and 28%, respectively [8–13]. However, the ionic crystal nature and dynamic ligand binding behavior of PeQDs lead to abundant surface defects, disordered carrier transport, and severe non-radiative recombination, which inevitably degrade the optoelectronic performance and long-term stability of PeQLEDs [7,14–16]. Therefore, rational surface ligand engineering is urgently required to passivate lattice defects, reduce non-radiative recombination centers, and enhance carrier transportation.

Conventional PeQDs synthesis primarily relies on long-chain organic ligands to ensure the sufficient precursor dissolution, regulate the crystallization and growth of PeQDs, and maintain the colloidal stability of the resulting PeQDs [17–19]. However, due to the weak and dynamic binding interaction between the commonly used long-chain ligands (oleic acid/oleylamine, OA/OAm) and PeQD surfaces, these ligands are prone to desorb from the surface during multiple centrifugation and

* Corresponding authors.
E-mail addresses: liufy@swjtu.edu.cn (F. Liu), liwen3337@swjtu.edu.cn (W. Li).
[1] These authors contributed equally to the work.

https://doi.org/10.1016/j.jallcom.2026.189991
Received 8 May 2026; Received in revised form 14 July 2026; Accepted 21 July 2026
Available online 22 July 2026
0925-8388/© 2026 Elsevier B.V. All rights are reserved, including those for text and data mining, AI training, and similar technologies.

purification processes [14,20]. Such ligand detachment is often accompanied by the loss of surface halide ions, leading to the formation of imperfect $PbBr_6^{4-}$ octahedra and abundant dangling bonds on the surface of PeQDs [21–23]. These surface defects act as efficient non-radiative recombination centers and accelerate the phase transition, ultimately causing severe photoluminescence quenching of PeQDs [24]. Furthermore, the inherent insulating nature of the OA/OAm ligands inevitably hinders efficient carrier injection/transport in devices, leading to degraded performance of PeQLEDs.

To address these problems, various strategies including ligand exchange, in-situ ligand compensation, and multi-ligand synergistic modification have been developed to improve the crystal quality and conductivity of PeQDs [19,25–27]. For example, a series of conjugated small-molecule ligands derived from 3-phenyl−2-propen−1-amine bromide with varied functional substituents have been employed for ligand exchange, which effectively enhances carrier mobility and conductivity [17]. An in-situ surface passivation strategy using benzhydroxamic acid during PeQD fabrication has also been developed, enabling $FAPbBr_3$ QDs to achieve a photoluminescence quantum yield (PLQY) as high as 92.5% [18]. Additionally, a ternary ligand system combining tributyl phosphate oxide (TBPO), dodecyl dimethyl ammonium bromide (DDAB), and $Ca(SCN)_2$ has been designed for post-treatment ligand exchange, effectively reducing the defect density and improving electron mobility of nanocrystal films [28]. Nevertheless, despite these ligands strategies can improve the optoelectronic properties of PeQDs, their alkyl chains are insulating and usually have a single-dentate coordination, resulting in limited enhancement of charge transport and systematic investigations on the influence of ligand modification on carrier transport and recombination dynamics in PeQLEDs remain insufficient [29,30]. In contrast, aromatic sulfonic acids possess strong coordination, structural rigidity, and π-conjugated systems. $-SO_3^-$ provides strong Lewis basicity for coordination with Pb^{2+}, while the substituents on the aromatic ring can regulate molecular polarization and achieve bidirectional carrier transport, which is something simple thiol ligands cannot achieve. Therefore, the exploration of suitable surface ligands that can simultaneously passivate surface

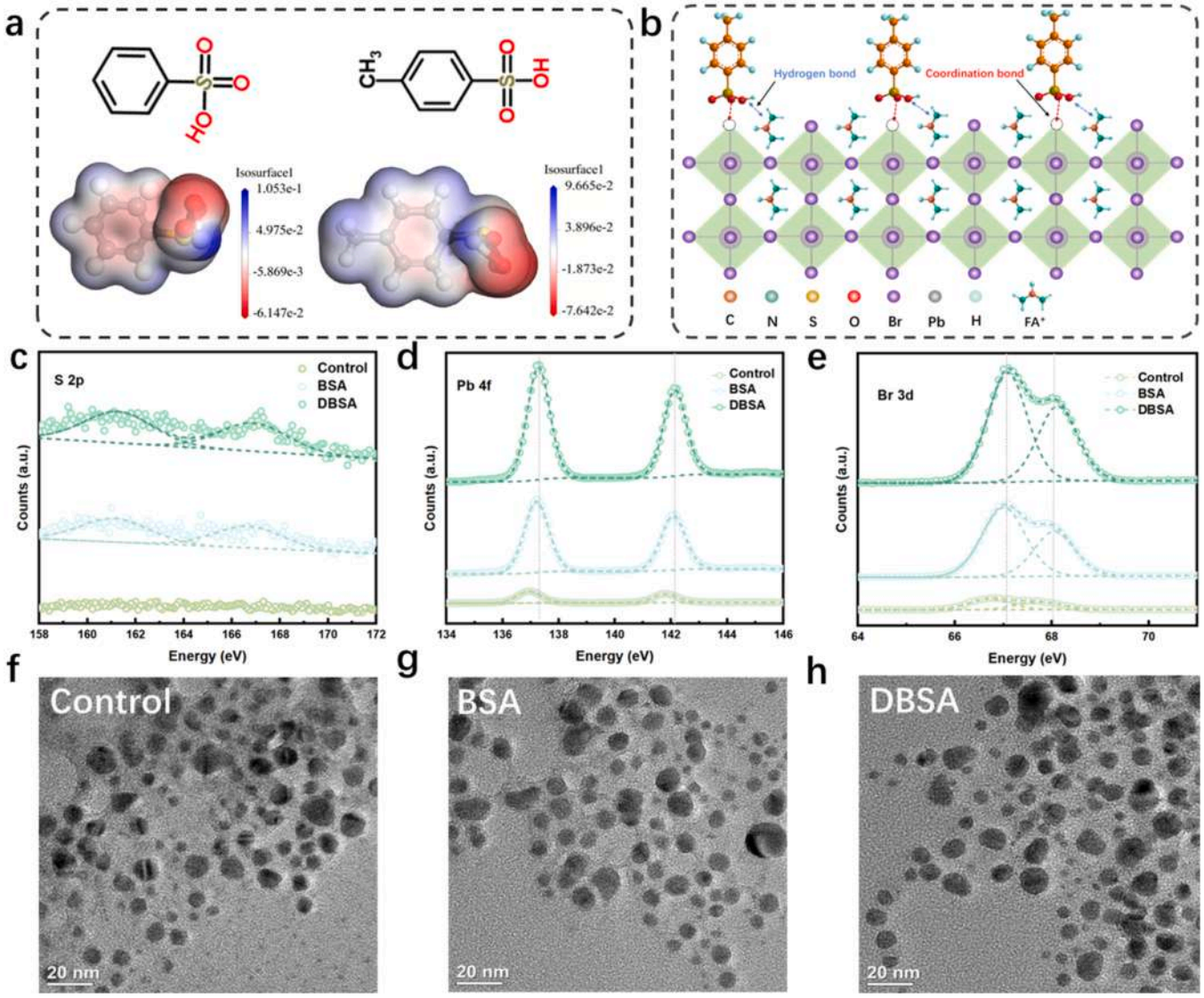


Fig. 1. a) Chemical structure and simulated electrostatic potential profiles of BSA and DBSA molecules. b) Schematic illustration of the binding property of DBSA at the surface of $FAPbBr_3$ PeQDs. c-e) XPS spectra of S 2*p* (c), Pb 4 *f* (d), and Br 3*d* (e) of control, BSA and DBSA-PeQDs. f-h) TEM images of (f) control, (g) BSA and (h) DBSA-PeQDs.

defects of PeQDs and regulate carrier transport behavior is highly desirable for achieving high-performance PeQLEDs.

Herein, we employed benzenesulfonic acid (BSA) and p-toluenesulfonic acid (DBSA) as small molecule ligands to modulate the surface properties and electrical performance of $FAPbBr_3$ QDs. The sulfonic acid groups of both ligands offer multiple chelating sites that strongly interact with the surface of PeQDs, reducing ligands loss during purification and enhancing the crystal quality of QDs. Electrical characterization further indicates that the emissive layer based on DBSA-PeQDs exhibits superior carrier transport properties, originated from the methyl substituent which enhances molecular polarization and facilitates rapid charge transport along the π-conjugated backbone. As a result, DBSA-based PeQLEDs achieved a low turn-on voltage of 2.2 V, a maximum EQE of 17.44%, and a peak luminance of 45,069 cd m^{-2}. These values represent significant improvements over the control device with a turn-on voltage of 3.1 V, an EQE of 14.06%, and a luminance of 23,776 cd m^{-2}. This work provides new insights into the rational design of surface ligands for tailoring QDs surface properties and carrier transport, paving the way for achieving high-performance PeQLEDs.

2. Results and discussion

The pristine $FAPbBr_3$ PeQDs were synthesized by using the commonly ligand-assisted reprecipitation (LARP) method [31,32]. To optimize the QDs, a certain amount of BSA and DBSA powder was added to the solvent of the pristine synthesis method. Detailed information is described in the experimental section. The corresponding chemical structures and simulated electrostatic potential curves (EPS) of BSA and DBSA are shown in Fig. 1a. The EPS analysis indicates that the electrons are mainly located around the oxygen atoms, suggesting that they may combine with the uncoordinated Pb atoms on the surface of PeNCs through Lewis acid-base reactions. Moreover, the electron-deficient atom of hydrogen in the hydroxyl (-OH) group can form hydrogen bonds with the FA^+ and Br^- ions respectively to enhance the interaction and eliminate surface defects, thereby improving the overall stability of the PeQDs (Fig. 1b) [18,23].

The interactions between BSA and DBSA molecules and PeQDs was investigated by X-ray photoelectron spectroscopy (XPS) measurement. The S 2p and O1s spectra in Fig. 1c revealed distinct features of the sulfonic groups originating from BSA and DBSA molecules, verifying the existence of BSA and DBSA in the optimized PeQDs. Meanwhile, the peaks of Pb 4 f and Br 3d spectra shifted towards higher binding energies, indicating a strong interaction between the Pb^{2+} and Br^- ions and the electronegative sulfonic groups of BSA and DBSA molecules (Fig. 1d and e) [33]. Additionally, a shift of the N1s peak to a higher binding energy provides direct evidence that the BSA and DBSA molecules stabilize PeQDs by interaction with FA^+ ions in the local chemical environment (Figure S1). The FTIR spectrum shows that both the control and optimized PeQDs exhibit characteristic peaks of -COOH and $-NH_2$. Meanwhile, the pure DBSA ligand shows two typical strong peaks of S═O asymmetric and symmetric stretching vibrations at ~1120 cm^{-1} and ~1060 cm^{-1} . In the PeQDs samples modified by DBSA and BSA, the S═O peak shifts towards a lower wavenumber. These changes directly prove that the sulfonic acid group forms a coordination bond with the unsaturated Pb^{2+} on the PeQDs surface, rather than simple physical adsorption (Figure S2). Figure f-h shows the transmission electron microscopy (TEM) images of the control and target PeQDs. The control PeQDs have an average size of 12.9 nm, while the target PeQDs a more uniform size distribution with a smaller average size of 10.9 nm. Meanwhile, compared with the control-PeQDs, the SEM images of BSA-PeQDs and DBSA-PeQDs are also denser and more uniform morphology with obviously reduced QDs agglomeration (Figure S3). Correspondingly, atomic force microscope (AFM) results show that the root-mean-square (RMS) roughness of BSA-PeQDs (10.8 nm) and DBSA-PeQDs (8.26 nm) is significantly lower than that of control-PeQDs (12.7 nm) as shown in Figure S4. X-ray diffraction (XRD) analysis reveals strong peaks at 14.8° and 29.8°, corresponding to the (100) and (200) lattice planes (Figure S5), indicating that both control and target PeQDs exhibit a cubic perovskite phase (space group Pm3m) [34,35]. Additionally, the increased intensities are observed for the main diffraction peaks of the DBSA-PeQDs, suggesting the well-enhanced crystallinity of the PeQDs with DBSA incorporation.

We further compared the luminescent properties of the control and target PeQDs. The UV–vis absorption spectra indicated that the three PeQDs presented similar absorption spectra, and the Tauc plots showed a slight reduction in the band gap of BSA-PeQDs and DBSA-PeQDs (Figure S6). Furthermore, the UV–vis absorption spectra of neat BSA and DBSA show that neither ligand exhibits discernible absorption band in the visible region (particularly near 600 nm), indicating that the weak feature observed in the modified PeQD films is not associated with ligand-intrinsic absorption (Figure S6b). However, the PL emission intensities of target PeQDs are slightly enhanced relative to Control-PeQDs, (Figure2a). This tendency is further supported by the corresponding photoluminescence quantum yields (PLQYs), which are measured to be 79.81%, 82.47%, 96.93% for the control, BSA, and DBSA-PeQDs, respectively (Figure S7). This enhancement may be attributed to stronger adsorption of DBSA ligands on the QD surface, which strengthens interfacial interactions and more effectively passivates surface defects. The binding energies (E_B) between the QD surfaces and BSA and DBSA ligands were further calculated, determined to be −0.3313 eV, and −0.7854 eV, respectively (Figure S8). This indicates that the interaction between DBSA and the surface of QDs is stronger than that of BSA ligands, which may lead to an increase in surface coverage. These results are also consistent with the extended PL lifetime of BSA (τ_{avg}=7.39 ns) and DBSA-PeQDs (τ_{avg}=39.64 ns) (Fig. 2b, Table S2). Furthermore, space-charge limited-current (SCLC) measurements were performed on HODs to quantitatively evaluate the trap state density of the control and target PeQDs films (Fig. 2c). The extracted trap filling limiting voltage (V_{TFL}) for the control, BSA, and DBSA-PeQDs are 1.82 V, 1.61 V, 1.20 V, respectively. The trap density n_t was estimated using the equation $n_t = 2\varepsilon\varepsilon_0 V_{TFL}/eL^2$, where e is the elementary charge, L is the thickness of the EML layer (~40 nm), ε is the dielectric constant, and ε_0 represents the vacuum permittivity. the defect densities were calculated to be 1.71×10^{18} cm^{-3}, 1.51×10^{18} cm^{-3}, and 1.13×10^{18} cm^{-3} for the control, BSA, and DBSA-PeQDs devices, respectively [36,37]. The DBSA-PeQDs exhibits the lowest defect densities, illustrating that DBSA ligands are more strongly bond to the surface of the QDs, thereby suppressing the formation of surface defects caused by ligand desorption. Moreover, the scan-rate-dependent J-V measurements show that the BSA- and DBSA-PeQDs devices exhibited significant current hysteresis at any of the scan rates, and the V_{TFL} baseline changed very little with the scan rate, indicating that the ion migration was effectively suppressed (Figure S11).

The temperature-dependent photoluminescence (PL) spectroscopic measurement was used to investigate the non-radiative relaxation process and charge-phonon coupling behavior of PeQDs film. By fitting the full-width-at-half-maximum (FWHM) curves extracted from the two-dimensional (2D) temperature-dependent PL maps (Fig. 2d-f), the experimental data were found to be in good agreement with the best-fit curves ($R^2 > 0.99$). Quantitative evaluation of the charge phonon coupling strength of PeQDs films, was achieved by fitting the temperature-dependent FWHM using the Frohlich formula [38,39]:

$$\Gamma(T) = \Gamma_0 + \Gamma_{AC} + \Gamma_{LO} = \Gamma_0 + \gamma_{AC}T + \gamma_{LO} / [e^{E_{LO}/k_B T} - 1] \quad (1)$$

Wherein Γ_0 represents temperature-independent intrinsic inhomogeneous broadening, arising from the scattering due to structural disorder and defect. The homogeneous broadening components Γ_{AC} and Γ_{LO} correspond to acoustic (AC) and longitudinal optical (LO) phonon scattering contributions, where $\gamma_{AC}$and γ_{LO} denote the corresponding coupling strength, respectively. E_{LO} represents the LO-phonon energy and k_B is the Boltzmann constant. Near room temperature, LO-phonons

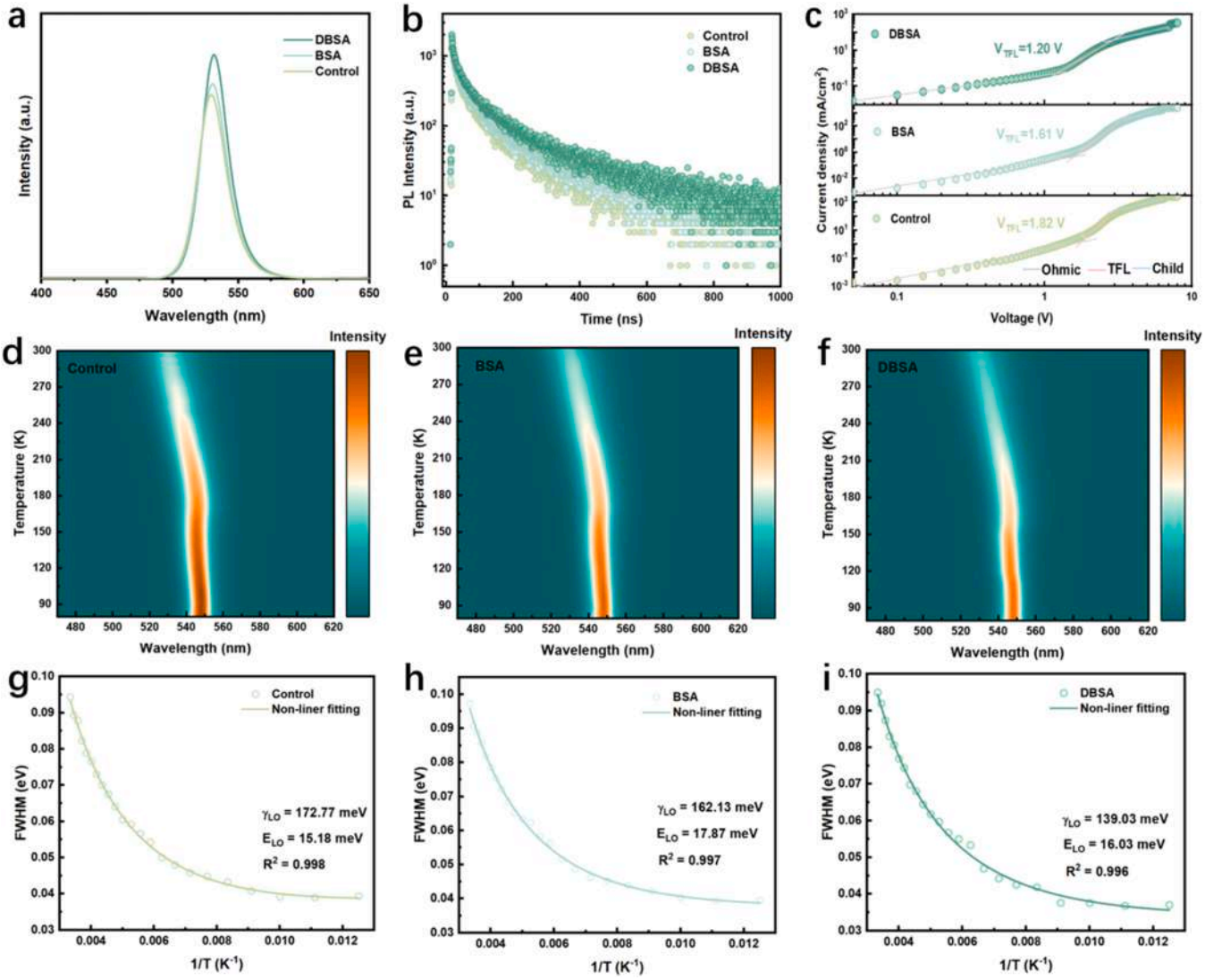


Fig. 2. a) PL emission and b) time-resolved PL decay spectra of control, BSA and DBSA-PeQDs films c) Current density–voltage (*J-V*) characteristics of ITO/HTL/$FAPbBr_3$/MoO_3/Al hole-only devices (HODs). d-f) Two-dimension (2D) temperature-dependent PL spectra of (d) control, (e) BSA and (f) DBSA-PeQDs films. g-i) FWHM of reciprocal temperature of (g) control, (h) BSA and (i) DBSA-PeQDs films.

are emitted sufficiently by high energy electrons. Therefore, the scattering from LO-phonons via the Fröhlich interaction is the dominant source of charge phonon coupling near room temperature, with scattering off AC phonons negligible [40,41]. Correspondingly, our analysis focused on evaluating variations of γ_{LO} and $E_{LO}$of PeQDs films. By fitting the FWHM curves extracted from the two-dimensional (2D) temperature-dependent PL maps (Fig. 2d-f), excellent consistency was achieved between experimental data and theoretical simulations ($R^2 >$ 0.99). The coupling strength γ_{LO} was determined to be 139.03 meV for DBSA-PeQDs films , 162.13 meV for BSA-PeQDs films and 172.77 meV for Control-PeQDs films (Fig. 2g-i). The detailed fitting parameters are listed in Table S1. Notably, this reduction may be attributed to the stronger interaction between DBSA and the surface of PeQDs. Such strong binding suppresses surface phonon generation and alleviates charge-phonon coupling, consequently diminishing nonradiative energy dissipation pathways of excited states.

To explore the influence of BSA and DBSA on the carrier dynamic behavior of PeQLEDs, the dielectric properties of control and target PeQDs films were further evaluated. The quantitative ESP values around the sulfonic oxygen region indicate that the oxygen atoms in DBSA are slightly more negative than those in BSA (approximately −0.07642 eV for DBSA and −0.06147 eV for BSA) (Fig. 1a).The methyl substituent changes the spatial distribution of electrostatic potential over the entire aromatic sulfonic acid molecule, creating a more polarized molecular framework with an electron-rich sulfonic acid end and an electron-donating methyl-substituted aromatic end. Meanwhile, in the UV–vis absorption spectrum (Figure S6), the UV–vis absorption edge of the DBSA-PeQDs film redshifts compared to the BSA-PeQDs film, and the band gap shrinks, reflecting that the methyl group enhances the delocalization of π electrons through the electron donor conjugation effect. Therefore, the DBSA molecule has a stronger surface binding and an enhanced overall molecular polarization combined effect with the quantum dots, which enables efficient bidirectional carrier transport within PeQD films. HODs with the structure of ITO/CZTS/PTAA/$FAPbBr_3$ QDs/MoO_3/Al were fabricated, the current density-voltage (*J-V*) curves of these HODs demonstrate that the BSA and DBSA modified devices exhibit considerably higher current densities than the control device, with the DBSA-based device achieving the highest hole current density (Fig. 3a). We further quantified the carrier mobility of the PeQDs films using SCLC analysis (Fig. 3b). In the Child region, the carrier mobility was determined by the Mott-Gurney equation $\mu = 8JL^3/9\varepsilon\varepsilon_0V^2$ [42,43]. The hole mobility of the control PeQDs film was calculated to be 2.36×10^{-5} $cm^2V^{-1}s^{-1}$, which was significantly enhanced after the modification with BSA and DBSA. Specifically, the hole mobility of the

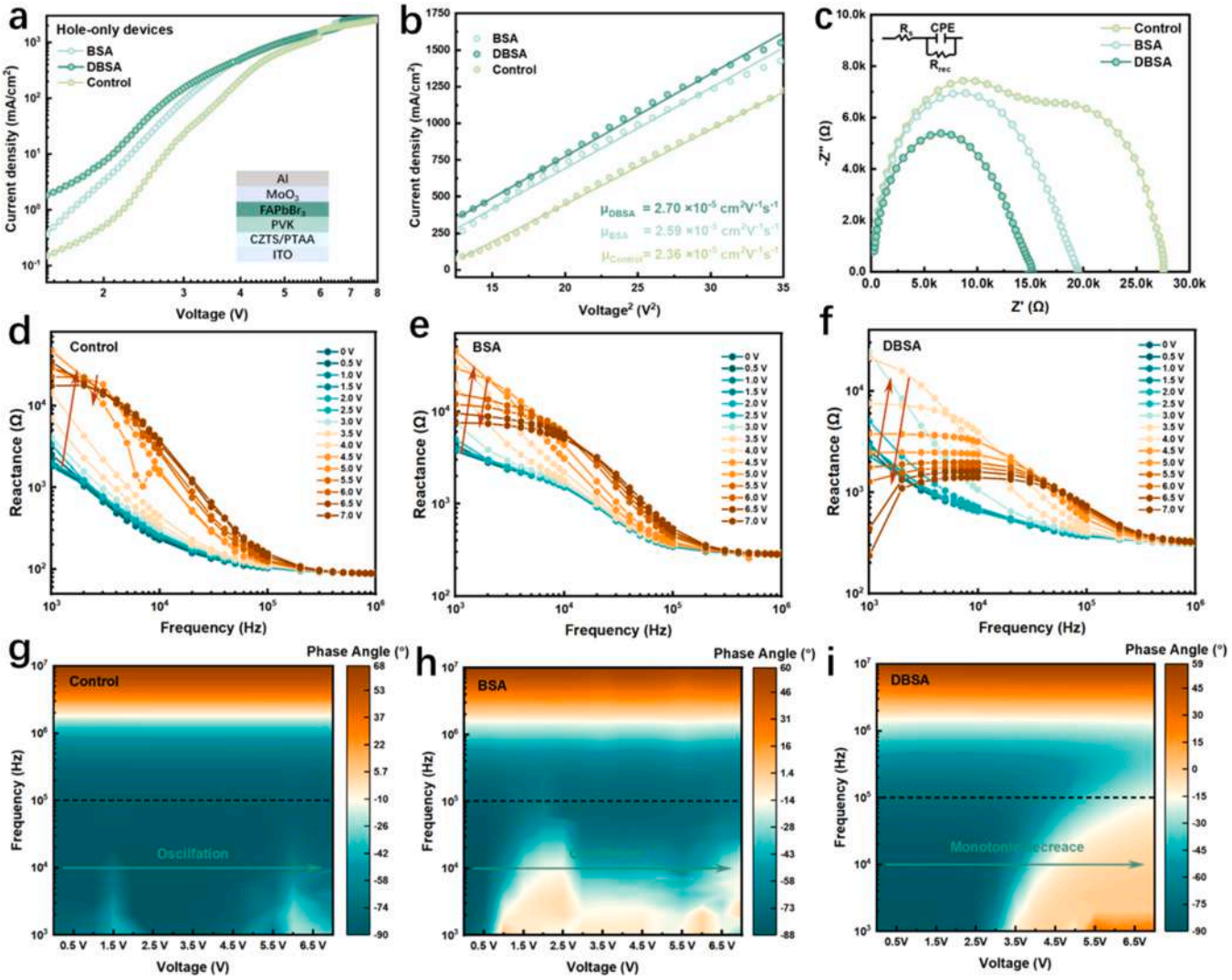


Fig. 3. a) HODs and b) scatter plots of *J-V*^{2} in the child region of HODs based on control, BSA and DBSA PeQDs films. c) Nyquist plots of impedance spectra. d-f) reactance of (d) control, (e) BSA and (f) DBSA PeQLEDs. g-i) phase angle of (g) control, (h) BSA and (i) DBSA PeQLEDs.

DBSA-PeQDs film (2.70×10^{-5} cm^{2}V^{-1}s^{-1}) was higher than that of the BSA-PeQDs film (2.59×10^{-5} cm^{2}V^{-1}s^{-1}). These results mean that the electronic nature of the methyl substituent in the DBSA ligands plays a key role in promoting carrie transport in PeQDs films. Electrochemical impedance spectroscopy (EIS) measurement was further utilized to examine the charge transport and recombination behavior. The corresponding Nyquist plots can be well fitted using an equivalent circuit model consisting of a series resistance (R_s), a recombination resistance (R_{rec}), and a correlated capacitance, as shown in the inset of Fig. 3c. In Fig. 3c, the DBSA-based PeQLEDs presents a smaller semicircular radius and lower R_{rec}, signifying easier charge transport as arising from the combined effects of stronger surface binding, enhanced molecular polarization and better film morphology. [42,44].

Having established the effects of BSA and DBSA ligands on charge transport behavior, we further analyze the discrepancies in carrier recombination dynamics within PeQLEDs based on control and target PeQDs by impedance spectra. As presented in Figures S9a, at frequencies below 10^4 Hz, the impedance of the control-based PeQLEDs declines from 9.72×10^4 Ω to 1.86×10^4 Ω at 10^3 Hz with increasing voltage, followed by a subsequent rebound to 4.95×10^4 Ω at 10^3 Hz. A more pronounced impedance evolution is observed in BSA-based PeQLEDs, where the impedance drops from 9.74×10^4 Ω to 2.34×10^3 Ω after successive oscillations at 10^3 Hz (Figures S9b). In sharp contrast, the impedance of DBSA-based PeQLEDs decreases monotonically with rising voltage at a considerably faster rate, declining from 8.30×10^4 Ω at 0 V to merely 65.63 Ω at 7.0 V measured at 10^3 Hz (Figures S9c). This observation manifests that DBSA-based PeQLEDs possess significantly suppressed charge accumulation and diminished energy loss, achieving more efficient radiative recombination [45,46]. As depicted in Fig. 3d-f, the reactance first rises and then declines with increasing voltage, and this trend being more pronounced at low frequencies. The change in reactance is caused by the alteration of the capacitance characteristics of the device. Notably, for the control-based PeQLEDs, the reactance reaches a maximum value of 4.73×10^4 Ω at 5.0 V and then begins to decrease, reaching a minimum value of 1.76×10^4 Ω at 7 V and 10^3 Hz. Meanwhile, severe charge accumulation and inferior recombination efficiency give rise to irregular fluctuations in reactance from 4.5 V to 7 V at frequencies below 10^4 Hz. For BSA-based PeQLEDs, defects suppression leads reduced capacitive charge storage, yielding a reactance of 4.53×10^4 Ω at 4.5 V and 10^3 Hz. As the voltage continues to increase, the reactance shows a monotonic downward trend, falling to 7.58×10^3 Ω at 7 V, thereby alleviating interfacial charge accumulation during device operation. In comparison, the DBSA-based PeQLEDs shows a more remarkable change. The reactance reaches its maximum value of 2.15×10^4 Ω at 3.5 V and 10^3 Hz, and then decreases monotonically and rapidly to 236.44 Ω at 7 V as the voltage increases. This rapid decay may

be attributed to the synergistic effects of defect passivation and the reduction of interfacial charge accumulation, which indirectly mitigates the loss of energy utilization efficiency caused by charge congestion and nonradiative recombination [31,47]. By analyzing the multi-scale phase angle responses of the three types of devices, the differences in energy loss during the carrier transport and recombination processes can be more clearly elucidated. In the control device, as shown in Fig. 3g, the phase angle decreases with increasing voltage at frequencies below 10^5 Hz, but the change is relatively small and accompanied by significant oscillations. The BSA-based device exhibits a similar trend, but with greater magnitude of change and more pronounced oscillations (Fig. 3h). The irregular low-frequency phase-angle oscillations in the control and BSA-based devices indicate distributed relaxation processes associated with interfacial charge accumulation, trap-assisted carrier relaxation and non-uniform transport pathways. By contrast, as shown in Fig. 3i, the DBSA-based device exhibits a more monotonic and stable phase-angle evolution over the low-frequency region, suggesting a narrower distribution of relaxation processes and more efficient carrier transport [47]. This interpretation is consistent with the reduced trap density, higher hole mobility, lower recombination resistance and faster impedance/reactance decay of the DBSA-based device.

Given the superior defect passivation and enhanced charge transport capabilities of BSA and DBSA modified PeQDs, we incorporated Control, BSA, and DBSA PeQDs as the emissive layer to construct PeQLEDs with a device structure of ITO/CZTS/PTAA/$FAPbBr_3$ QDs/PO-T2T/LiF/Al (Fig. 4a). The corresponding device energy level diagram is illustrated in Fig. 4b. The ultraviolet photoelectron spectroscopy results show that the HOMO energy levels of the control, BSA, and DBSA-PeQD films are 5.97 eV, 5.89 eV, and 5.68 eV respectively (Figure S10). This indicates that the hole injection barrier of the BSA and DBSA-modified PeQD has been significantly reduced. Concurrently, To reduce the hole injection barrier, an inorganic layer CZTS with deep valence-band maximum was adopted as the hole injection layer, coupled with poly(bis(4-phenyl) (2,4,6-trimethyl-phenyl) amine) (PTAA) as an interface layer to improve the optoelectronic performance of PeQLEDs. Figs. 4c and 4d display the current density-voltage-luminance (*J-V-L*) and current efficiency *(CE)-J* curves of the three PeQLEDs, respectively. The turn-on voltage is reduced from 3.2 V for the control-based PeQLEDs to 2.2 V for both BSA and DBSA-based PeQLEDs, signifying enhanced carrier transport. Additionally, the leakage current of BSA and DBSA-based PeQLEDs was significantly suppressed, which is attributed to the smoother surface morphology in the BSA and DBSA-PeQDs films. The maximum brightness (L_{max}) of control-based PeQLEDs is 23,776 cd m^{-2}, while the L_{max} of BSA and DBSA-based PeQLEDs is elevated to 31,518 cd m^{-2} and 45,069 cd m^{-2}, respectively. This enhancement is attributed to enhanced carrier mobility and accelerated radiative recombination rate of PeQDs. Meanwhile, the *CE* increased from 45.81 Cd/A of control-based PeQLEDs to 75.31 Cd/A of BSA-based PeQLEDs and 84.22 Cd/A of DBSA-based PeQLEDs, while the EQE increased from 14.06% of control-based PeQLEDs to 16.01% of BSA-based PeQLEDs and 17.44% of DBSA-based PeQLEDs (Fig. 4e). Notably, this also represents the current highest EQE achieved by PeLEDs using CZTS as the hole injection layer. Fig. 4f shows the EQE_{max} statistics for 30 devices of three types PeQLEDs. The average peak EQE for DBSA-based PeQLEDs is 16.4%, substantially outperforming the control-based PeQLEDs (12.8%) and BSA-based PeQLEDs (14.9%).

3. Conclusions

In conclusion, we exploited the strong interactions between BSA and DBSA ligands and the surface of $FAPbBr_3$ QDs to realize efficient defects passivation and improved structural stability, thus endowing the QDs with superior optical properties. Additionally, single-carrier devices confirmed that DBSA polarized molecule with electron-donating groups show more pronounced improvements in charge transport characteristics of PeQDs. Furthermore, the multi-scale responses of reactance, impedance, and phase angle from an energetic perspective validated that DBSA-based devices exhibit lower carrier transport impedance, suppressed oscillations, and improved recombination efficiency. Therefore, the PeQLEDs based on DBSA ligands exhibited the best device performance, achieving a maximum EQE of 17.44% and a peak luminance of 45,069 cd m^{-2} at 529 nm. This work highlights the effectiveness of ligand engineering in improving the surface quality of PeQDs and enhancing their charge transport capabilities. Meanwhile, the EQE

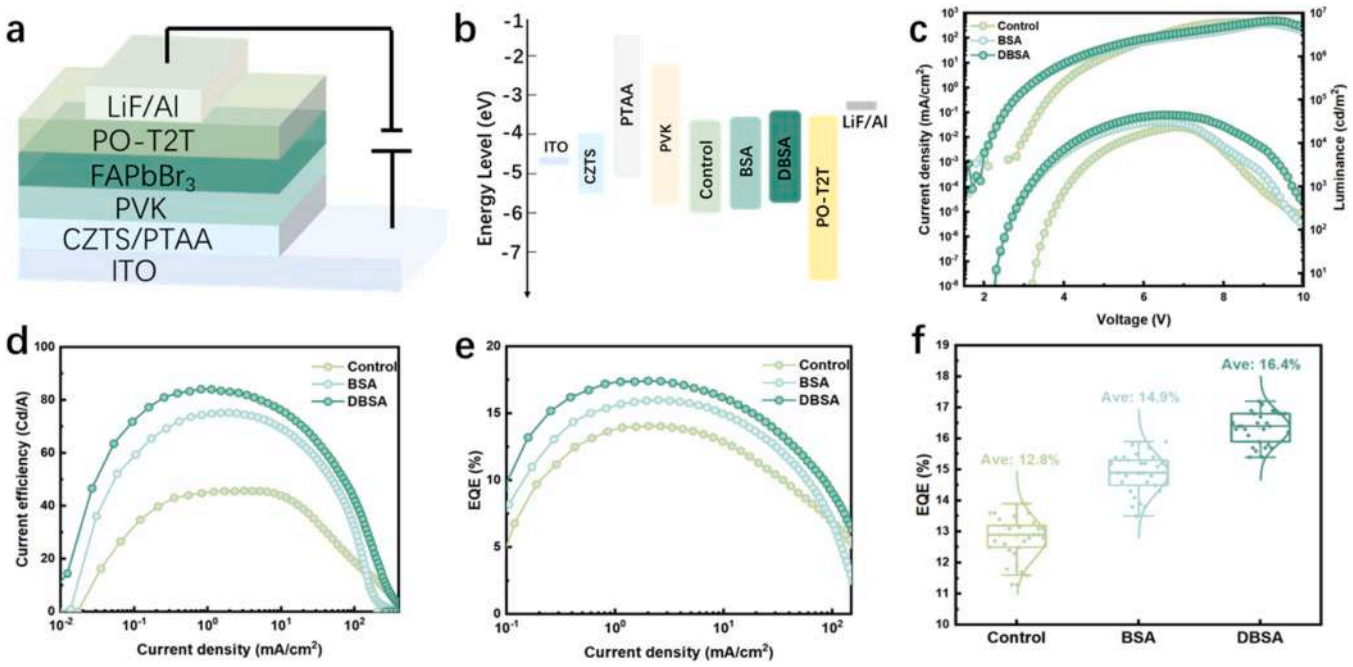


Fig. 4. a) Schematic illustration of PeQLEDs structure. b) Energy level diagram for different component layers in PeQLEDs. c) Current density-voltage-luminance (*J-V-L*) curves, d) Current efficiency-current density (*CE-J*) curves, e) EQE-current density curves, f) Statistics of EQE of 30 devices based on control, BSA and DBSA PeQLEDs.

improvement is primarily assigned to defect passivation and improved carrier transport based on the available data, while possible optical-outcoupling contributions cannot be fully excluded without dedicated transition dipole moment (TDM) measurements. It provides valuable insights and guidance on modulating substituents to simultaneously improve the crystal quality and carrier transport properties of PeQDs for high-performance LEDs.

4. Experimental section

Materials: Copper acetate ($Cu(CH_3COO)_2{\cdot}H_2O$), zinc acetate ($Zn(CH_3COO)_2$), stannous chloride ($SnCl_2{\cdot}2\,H_2O$), thiourea, iso-propyl alcohol ($(CH_3)_2CHOH$) were obtained from Shanghai Macklin Co, Ltd. Keshi provided ethanol, 2-Methoxyethanol (98%), toluene (99.9%), 1-butanol(98%), octane (98%) and N,N-Dimethylformamide (DMF, 98%). Additionally, molybdenum trioxide (MoO_3, 99.95%), oleic acid (OA, 90%) and LiF were sourced from Shanghai Aladdin Industrial Corporation Co., Ltd. Xi'an Polymer Light Technology Corp supplied lead bromide ($PbBr_2$), formamidine bromide (FABr), poly(bis(4-phenyl)(2,4,6-trimethyl-phenyl) amine) (PTAA,99.9%)and (1,3,5-triazine−2,4,6-triyl)tris(benzene−3,1-diyl)tris(diphenylphosphine oxide) (PO-T2T, 99.9%).

Preparation of $FAPbBr_3$ QDs: The synthesis of $FAPbBr_3$ QDs was carried out using a modified method based on literature. The $FAPbBr_3$ precursor (150 μL), prepared by dissolving $PbBr_2$ and FABr in DMF with a molar ratio of 1:2.2 and Pb^{2+} concentration at 0.2 M, was injected into a vial containing a crystallization-inducing solution composed of 5 mL of toluene, 2 mL of 1-butanol, 500 μL of oleic acid, and 30 μL of n-diacylamine. The solution was vigorously stirred for 10 min after the injection, following which it was centrifuged at 13000 rpm for 5 min and the supernatant was discarded. The precipitate was redispersed in 1 mL of n-hexane and then centrifuged at 2000 rpm for 2 min. The resulting supernatant was filtered through a 0.22 μm PTFE filter to collect $FAPbBr_3$ QDs. Prior to the injection of the precursor, the crystallization-inducing solution was precooled to 8–10 °C.

Preparation of target $FAPbBr_3$ QDs: The synthesis processes for BSA-modified and DBSA- modified $FAPbBr_3$ QDs are the same as those for the control $FAPbBr_3$ QDs, except that BSA (10 mg) and DBSA (10 mg) were added to the crystallization-inducing solution.

Preparation of CZTS films: CZTS precursor solution was prepared by sequentially dissolving $Cu(CH_3COO)_2{\cdot}H_2O$ (0.6 mmol), $SnCl_2{\cdot}2\,H_2O$ (0.3 mmol), $Zn(CH_3COO)_2$ (0.3 mmol) and thiourea (6 mmol) in 20 mL 2-Methoxyethanol solvent under stirring at 50 °C. The precursor film was spin-coated (2000 rpm, 30 s) once on patterned and cleaned ITO substrate and annealed at 300 °C for 5 min on a hot-stage in N_2 atmosphere. Note, an excess amount of thiourea is used for the purpose of getting the CZTS films with a composition close to stoichiometry, because a serious sulfur loss may occur during thermal decomposition.

Device fabrication: The PVK solutions (in chlorobenzene, 5 mg mL^{-1}) were spin-coated at 3000 r.p.m. for 30 s on the prepared CZTS films and baked at 150 °C for 20 min. Then, the PTAA (in chlorobenzene, 3 mg mL^{-1}) solution was spin-coated onto the PVK surface at a speed of 4000 r.p.m. for 30 s, and annealed at 150 °C for 10 min. $FAPbBr_3$ QDs were spin-coated at 1000 rpm for 60 s on the PTAA films and then quickly transferred into a high-vacuum evaporator without annealing. Afterward, in a low-vacuum environment of 8×10^{-5} Pa, a sequential deposition of 50 nm PO-T2T, 1 nm of LiF, and 80 nm of Al was carried out. The hole-only device was fabricated by sequentially depositing 3 nm of MoO_3 and 80 nm of Ag onto perovskite film.

Characterizations: The crystalline structure and quality of the CZTS nanocrystal films were investigated by X-ray diffraction (XRD; X'Pert ProX-ray diffractometer) employing a Cu Kα (λ = 1.5418 Å) and Raman spectroscopy (Renishaw) using an Argon-ion laser (wavelength of 514.5 nm) at room temperature. The Raman spectra were acquired at a constant incident laser power of 2.5 mW. A JEOL JSM−7800 Prime scanning electron microscopy (SEM) with an accelerating voltage of 5 kV and atomic force microscopy (AFM, Bruker NanoScope V) with peak force tapping mode using silicon tips (TESP, Veeco) were used to characterize the morphologies of the films. The UV absorption spectra were obtained by UV−2500 (Shimadzu Corporation). The PL spectra, TRPL spectra, and temperature-dependent photoluminescence spectra were investigated using FLS980 (Edinburgh Instruments) spectrometer with a 450 W Xenon lamp. The room-temperature absolute PLQY of the films was measured on Edinburgh-FLS 980 spectrometer by an integrating sphere. Fourier transform infrared (FTIR) spectroscopy patterns were obtained to determine the types and changes of functional groups in materials using a TENSOR II spectrometer (Bruker) with a spectral resolution of 4 cm^{-1} at a scanning frequency of 1 spectra min^{-1}. The characterizations of low- (f = 5 K) and high-frequency (f = 100 K) capacitance-voltage curves of PeQLEDs were performed by Keithley 4200. The Keithley 2400 source meter combined with a QE-Pro spectrometer (Ocean Optics), was employed to characterize the performances of PeQLEDs in the glove box. The intensity of electroluminescence was measured by a FOIS−1 integration sphere.

CRediT authorship contribution statement

Maolin Mu: Writing – review & editing, Writing – original draft, Visualization, Validation, Supervision, Software, Project administration, Methodology, Investigation, Formal analysis, Data curation, Conceptualization. **Wen Li:** Writing – review & editing, Visualization, Validation, Supervision, Software, Resources, Project administration, Methodology, Investigation, Funding acquisition, Formal analysis, Data curation, Conceptualization. **Xiankan Zeng:** Methodology, Formal analysis, Data curation, Conceptualization. **Lunyao Pan:** Visualization, Validation, Supervision, Funding acquisition, Formal analysis, Data curation, Conceptualization. **Xinning Wang:** Software, Data curation. **Di Shen:** Formal analysis, Data curation. **Fangyan Liu:** Supervision, Resources. **Weiqing Yang:** Resources, Project administration, Formal analysis, Data curation. **Yaolin Zhang:** Software, Conceptualization. **Chenglong Li:** Investigation, Data curation. **Yuqiang Huang:** Software, Data curation.

Declaration of Competing Interest

The authors declare that they have no known competing financial interests or personal relationships that could have appeared to influence the work reported in this paper.

Acknowledgments

This work was supported by the National Key Research and Development Program Young Scientist Project (2023YFB3405700), the Natural Science Foundation of Sichuan Province (2025ZNSFSC0145) and the Fundamental Research Funds for the Central Universities (2682024CX050 ; 2682026ZTPY020). The authors would like to thank the Analysis and Testing Center of Southwest Jiaotong University for supporting the XRD measurements.

Supporting information

UV−vis and UPS spectra; additional J-V characteristics of HOD; XRD patterns; XPS and FTIR spectra of perovskite films; top-view SEM images and AFM characterization of perovskite films; Impedance measurements of PeQLEDs; and additional tables.

Appendix A. Supporting information

Supplementary data associated with this article can be found in the online version at doi:10.1016/j.jallcom.2026.189991.

References

[1] C. Zhang, L.K. Ono, Y. Qi, Color/Spectral Stability of Mixed Halide Perovskite Light-Emitting Diodes, Adv. Funct. Mater. 34 (27) (2024) 2314762.

[2] M. Zhang, X. Ma, J.L. Esguerra, H. Yu, O. Hjelm, J. Li, F. Gao, Towards sustainable perovskite light-emitting diodes, Nat. Sustain. 8 (3) (2025) 315–324.

[3] Q. Zhang, D. Zhang, Z. Liao, Y.B. Cao, M. Kumar, S. Poddar, J. Han, Y. Hu, H. Lv, X. Mo, A.K. Srivastava, Z. Fan, Perovskite light-emitting diodes with quantum wires and nanorods, Adv. Mater. 37 (23) (2025) 2405418.

[4] Q. Shan, Y. Dong, H. Xiang, D. Yan, T. Hu, B. Yuan, H. Zhu, Y. Wang, H. Zeng, Perovskite quantum dots for the next-generation displays: progress and prospect, Adv. Funct. Mater. 34 (36) (2024) 2401284.

[5] J. Fan, C. Han, G. Yang, B. Song, R. Xu, C. Xiang, T. Zhang, L. Qian, Recent progress of quantum dots light-emitting diodes: materials, device structures, and display applications, Adv. Mater. 36 (37) (2024) 2312948.

[6] F. Cai, B. Bai, Q. Wu, R. Xu, C. Xiang, X. Yang, G. Jia, Z. Du, Blue quantum dot light-emitting diodes toward full-color displays: materials, devices, and large-scale fabrication, Nano Lett. 25 (1) (2025) 1–15.

[7] D. Chen, P.K. Ko, C.H.A. Li, B. Zou, P. Geng, L. Guo, J.E. Halpert, Amino acid-passivated pure red $CsPbI_3$ Quantum Dot LEDs, ACS Energy Lett. 8 (1) (2023) 410–416.

[8] Y. Nong, J. Yao, J. Li, L. Xu, Z. Yang, C. Li, J. Song, Boosting External Quantum Efficiency of Blue Perovskite QLEDs Exceeding 23% by Trifluoroacetate Passivation and Mixed Hole Transportation Design, Adv. Mater. 36 (27) (2024) 2402325.

[9] J. Wang, M. Li, B. Cai, H. Ren, W. Fan, L. Xu, J. Yao, S. Wang, J. Song, Matched electron-transport materials enabling efficient and stable perovskite quantum-dot-based light-emitting diodes, Angew. Chem. Int. Ed. 63 (42) (2024) e202410689.

[10] S.-C. Feng, Y. Shen, X.-M. Hu, Z.-H. Su, K. Zhang, B.-F. Wang, L.-X. Cao, F.-M. Xie, H.-Z. Li, X. Gao, J.-X. Tang, Y.-Q. Li, Efficient and stable red perovskite light-emitting diodes via thermodynamic crystallization control, Adv. Mater. 36 (44) (2024) 2410255.

[11] Gao, Y.; Cai, Q.; He, Y.; Zhang, D.; Cao, Q.; Zhu, M.; Ma, Z.; Zhao, B.; He, H.; Di, D.; Ye, Z.; Dai, X., Highly Efficient Blue Light-Emitting Diodes Based on Mixed-Halide Perovskites with Reduced Chlorine Defects. Science Advances 10 (29), eado5645.

[12] S.-Q. Sun, J.-W. Tai, W. He, Y.-J. Yu, Z.-Q. Feng, Q. Sun, K.-N. Tong, K. Shi, B.-C. Liu, M. Zhu, G. Wei, J. Fan, Y.-M. Xie, L.-S. Liao, M.-K. Fung, Enhancing light outcoupling efficiency via anisotropic low refractive index electron transporting materials for efficient perovskite light-emitting diodes, Adv. Mater. 36 (24) (2024) 2400421.

[13] Y. Feng, H. Li, M. Zhu, Y. Gao, Q. Cai, G. Lu, X. Dai, Z. Ye, H. He, Nucleophilic reaction-enabled chloride modification on cspbi3 quantum dots for pure red light-emitting diodes with efficiency exceeding 26, Angew. Chem. Int. Ed. 63 (11) (2024) e202318777.

[14] X. Zhou, M. Yang, C. Shen, L. Lian, L. Hou, J. Zhang, Synchronously Polishing the Lead-Rich Surface and Passivating Surface Defects of $CsPb(Br/I)_3$ Quantum Dots for High-Performance Pure-Red PeLEDs, Nano Lett. 24 (12) (2024) 3719–3726.

[15] Y. Li, M. Deng, X. Zhang, T. Xu, X. Wang, Z. Yao, Q. Wang, L. Qian, C. Xiang, Stable and Efficient $CsPbI_3$ Quantum-dot Light-Emitting Diodes with Strong Quantum Confinement, Nat. Commun. 15 (1) (2024) 5696.

[16] B. Xu, S. Yuan, L. Wang, X. Li, Z. Hu, H. Zeng, Highly efficient blue light-emitting diodes enabled by gradient core/shell-structured perovskite quantum dots, ACS Nano 19 (3) (2025) 3694–3704.

[17] C. Zhao, C. Zhu, Z. Xu, Q. Ma, F. Yuan, J. Li, J. Xi, L. Li, S. Wang, B. Jiao, Z. Wu, Boosting carrier transport via functionalized short-chain conjugated ligands enables efficient green perovskite quantum dot light-emitting diodes, Chem. Eng. J. 501 (2024) 157596.

[18] J. Zhang, D. Zhang, X. Zhou, L. Lian, C. Shen, C. Su, S. Fang, X. Liang, F. Yuan, L. Hou, Y.-X. Yuan, In-Situ Surface Repair of $FAPbBr_3$ quantum dots toward high-performance pure-green perovskite light-emitting diodes, Nano Lett. 24 (39) (2024) 12196–12203.

[19] B. Zhao, M. Vasilopoulou, A. Fakharuddin, F. Gao, A.R. b Mohd Yusoff, R. H. Friend, D. Di, Light management for perovskite light-emitting diodes, Nat. Nanotechnol. 18 (9) (2023) 981–992.

[20] Z. Qi, X. Mei, J. Wang, J. Qiu, W. Zheng, K. He, M. Zhang, X. Zhang, X. Zhang, Ligand-pinning induced size modulation of $CsPbI_3$ perovskite quantum dots for red light-emitting diodes, Adv. Funct. Mater. 34 (44) (2024) 2405679.

[21] J. Guo, M. Lu, X. Zhang, S. Sun, C. Han, Y. Zhang, X. Yang, S.V. Kershaw, W. Zheng, A.L. Rogach, Highly stable and efficient light-emitting diodes based on orthorhombic γ-$CsPbI_3$ Nanocrystals, ACS Nano 17 (10) (2023) 9290–9301.

[22] H. Li, Y. Feng, M. Zhu, Y. Gao, C. Fan, Q. Cui, Q. Cai, K. Yang, H. He, X. Dai, J. Huang, Z. Ye, Nanosurface-reconstructed perovskite for highly efficient and stable active-matrix light-emitting diode display, Nat. Nanotechnol. 19 (5) (2024) 638–645.

[23] W. Lu, Y. Wu, X. Li, J. Huang, A. Ali, J. Ren, Q. Shang, C. Li, G.V. Baryshnikov, B. Xu, Multifunctional dithiol crosslinking additive enables highly efficient and stable inkjet-printed perovskite quantum dot light-emitting diodes, Adv. Mater. (2025) e15555 (n/a (n/a)).

[24] H. Zhao, H. Chen, S. Bai, C. Kuang, X. Luo, P. Teng, C. Yin, P. Zeng, L. Hou, Y. Yang, L. Duan, F. Gao, M. Liu, High-brightness perovskite light-emitting diodes based on $FAPbBr_3$ nanocrystals with rationally designed aromatic ligands, ACS Energy Lett. 6 (7) (2021) 2395–2403.

[25] W.A. Dunlap-Shohl, N. Tabassum, P. Zhang, E. Shiby, D.N. Beratan, D.H. Waldeck, Electron-Donating Functional Groups Strengthen Ligand-induced Chiral Imprinting on $CsPbBr_3$ Quantum Dots, Sci. Rep. 14 (1) (2024) 336.

[26] J. Xue, R. Wang, L. Chen, S. Nuryyeva, T.-H. Han, T. Huang, S. Tan, J. Zhu, M. Wang, Z.-K. Wang, C. Zhang, J.-W. Lee, Y. Yang, A Small-Molecule "Charge Driver" enables Perovskite Quantum Dot Solar Cells with Efficiency Approaching 13, Adv. Mater. 31 (37) (2019) 1900111.

[27] C.H. Jang, Y.I. Kim, A.K. Harit, J.M. Ha, S. Park, Y.W. Noh, A.-y Lee, K.S. Kim, J. W. Jung, H.Y. Woo, M.H. Song, Multifunctional conjugated molecular additives for highly efficient perovskite light-emitting diodes, Adv. Mater. 35 (24) (2023) 2210511.

[28] J.-N. Yang, Z.-Y. Ma, J.-D. Luo, J.-J. Wang, C. Ye, Y. Zhou, Y.-C. Yin, X.-C. Ru, T. Chen, L.-Y. Li, L.-Z. Feng, K.-H. Song, J. Ge, Q. Zhang, H.-B. Yao, Pseudohalogen resurfaced $CsPbBr_3$ nanocrystals for bright, efficient, and stable green-light-emitting diodes, Nano Lett. 23 (8) (2023) 3385–3393.

[29] L. Zhang, X. Chen, M. Zhang, D. Kong, F. Huang, J. Tian, Antisolvent etching-driven surface reconstruction of perovskite quantum dots enabling efficient light-emitting diodes, ACS Energy Lett. 10 (9) (2025) 4518–4526.

[30] J. Wang, Z. Yang, Y. Chen, H. Zhang, Y. Chen, Y. Bai, X. Jiang, B. Liu, J. Hong, Z. Fang, J. Gao, Z. Zhou, R. Yu, X. Song, Z. Yuan, T. Guo, F. Li, Y. Chen, Z. Weng, Sulfonic acid ligands promote surface reconstruction of perovskite quantum dots for high-performance light-emitting diodes, Adv. Opt. Mater. 13 (8) (2025) 2402764.

[31] L. Pan, X. Zeng, Y. Qu, M. Mu, S. Yang, Y. Chen, C. Li, L. Dai, L. Tao, H. Xin, W. Li, W. Yang, Bidirectional inhibiting interfacial ion migration in the inorganic hole transport layer for perovskite light-emitting diodes, Small 20 (48) (2024) 2405528.

[32] H. Chen, L. Fan, R. Zhang, C. Bao, H. Zhao, W. Xiang, W. Liu, G. Niu, R. Guo, L. Zhang, L. Wang, High-efficiency formamidinium lead bromide perovskite nanocrystal-based light-emitting diodes fabricated via a surface defect self-passivation strategy, Adv. Opt. Mater. 8 (6) (2020) 1901390.

[33] J. Chen, X. Liu, B. Cai, Y. Cheng, H. Wen, D. Zhu, Y. Xiong, L. Dai, X. Yan, B. Xiang, X. Luo, W. Feng, J. Du, S. Dong, Q. Shan, S. Chen, H. Zeng, Q. Xiong, L. Duan, D. Ma, Lattice-matched molecular-anchor design for high-performance perovskite quantum dot light-emitting diodes, Nat. Commun. 16 (1) (2025) 8201.

[34] M. Mu, W. Li, L. Pan, X. Zeng, Q. Wang, Y. Chen, C. Li, D. Shen, X. Wang, S. Yang, H. Xin, W. Yang, Interface Bridge Engineering for High Efficient Hole Injection in CZTS-based perovskite light-emitting diodes, Adv. Opt. Mater. 13 (27) (2025) e01028.

[35] L. Pan, W. Li, X. Zeng, M. Mu, Q. Wang, Y. Chen, C. Li, S. Yang, L. Dai, L. Tao, W. Yang, Inorganic Cu_2ZnSnS_4 hole transport layer for perovskite light-emitting diodes, Inorg. Chem. Front. 11 (16) (2024) 5233–5243.

[36] V.M. Le Corre, Space-charge-limited current measurements: a problematic technique for metal halide perovskites, J. Phys. Chem. Lett. 15 (39) (2024) 10001–10008.

[37] E.A. Duijnstee, J.M. Ball, V.M. Le Corre, L.J.A. Koster, H.J. Snaith, J. Lim, Toward understanding space-charge limited current measurements on metal halide perovskites, ACS Energy Lett. 5 (2) (2020) 376–384.

[38] T.J. Savenije, C.S. Ponseca Jr., L. Kunneman, M. Abdellah, K. Zheng, Y. Tian, Q. Zhu, S.E. Canton, I.G. Scheblykin, T. Pullerits, A. Yartsev, V. Sundström, Thermally activated exciton dissociation and recombination control the carrier dynamics in organometal halide perovskite, J. Phys. Chem. Lett. 5 (13) (2014) 2189–2194.

[39] X. Zhou, Z. Ren, Z. Zheng, C. Luo, H. Chen, H. Peng, B. Hu, Y. Chen, Efficient and stable blue perovskite light-emitting diodes enabled by effective hydrolysis of dichloride, Adv. Funct. Mater. 35 (2) (2025) 2412894.

[40] A.D. Wright, C. Verdi, R.L. Milot, G.E. Eperon, M.A. Pérez-Osorio, H.J. Snaith, F. Giustino, M.B. Johnston, L.M. Herz, Electron–phonon coupling in hybrid lead halide perovskites, Nat. Commun. 7 (1) (2016) 11755.

[41] J. Cui, A.P. Beyler, I. Coropceanu, L. Cleary, T.R. Avila, Y. Chen, J.M. Cordero, S. L. Heathcote, D.K. Harris, O. Chen, J. Cao, M.G. Bawendi, Evolution of the Single-Nanocrystal Photoluminescence Linewidth with Size and Shell: Implications for Exciton–Phonon Coupling and the Optimization of Spectral Linewidths, Nano Lett. 16 (1) (2016) 289–296.

[42] J. Li, Y. Nong, J. Yao, L. Xu, Z. Yang, S. Wang, J. Song, Efficient Deep-Blue (465 nm) perovskite quantum dot-based light-emitting diodes via triphenylamine derivative tailored hole transport engineering, Adv. Funct. Mater. 35 (2) (2025) 2412367.

[43] Y.-F. Lan, J.-S. Yao, J.-N. Yang, Y.-H. Song, X.-C. Ru, Q. Zhang, L.-Z. Feng, T. Chen, K.-H. Song, H.-B. Yao, Spectrally Stable and Efficient Pure Red $CsPbI_3$ Quantum Dot Light-Emitting Diodes Enabled by Sequential Ligand Post-Treatment Strategy, Nano Lett. 21 (20) (2021) 8756–8763.

[44] B. Roose, K. Dey, M.R. Fitzsimmons, Y.-H. Chiang, P.J. Cameron, S.D. Stranks, Electrochemical impedance spectroscopy of all-perovskite tandem solar cells, ACS Energy Lett. 9 (2) (2024) 442–453.

[45] Y. Chen, C. Yan, Z. Chen, X. Zeng, Q. Wang, S. Yang, L. Pan, C. Li, M. Mu, W. Li, G. Tang, W. Yang, Interfacial coulomb-enhanced charge injection for efficient perovskite light-emitting diodes, Mater. Today Phys. 43 (2024) 101413.

[46] X. Xiao, T. Ye, J. Sun, X. Qu, Z. Ren, D. Wu, S. Ding, X.W. Sun, W.C.H. Choy, K. Wang, Capacitance–voltage characteristics of perovskite light-emitting diodes: modeling and implementing on the analysis of carrier behaviors, Appl. Phys. Lett. 120 (24) (2022) 243501.

[47] Y. Chen, X. Zeng, C. Yan, S. Yang, L. Pan, C. Li, M. Mu, W. Li, G. Tang, W. Yang, Suppressing leakage current and charge accumulation via perovskite interface morphology regulation for efficient light-emitting diodes, Chem. Eng. J. 495 (2024) 153520.